UKAEA-CCFE-PR(21)71

J. S Allcock, S. A. Silburn, R. M. Sharples, J .R.
Harrison, N. J. Conway, J. W. M. Vernimmen

2-D measurements of plasma electron density using coherence imaging with a pixelated phase mask

Enquiries about copyright and reproduction should in the first instance be addressed to the UKAEA Publications Officer, Culham Science Centre, Building K1/0/83 Abingdon, Oxfordshire, OX14 3DB, UK. The United Kingdom Atomic Energy Authority is the copyright holder.

The contents of this document and all other UKAEA Preprints, Reports and Conference Papers are available to view online free at scientific-publications.ukaea.uk/

2-D measurements of plasma electron density using coherence imaging with a pixelated phase mask

J. S Allcock, S. A. Silburn, R. M. Sharples, J .R. Harrison, N. J. Conway, J. W. M. Vernimmen

This is a preprint of a paper submitted for publication in
Review of Scientific Instruments

2-D measurements of plasma electron density using coherence imaging with a pixelated phase mask

J. S. Allcock,[1, 2, a)] S. A. Silburn,[2] R. M. Sharples,[1] J. R. Harrison,[2] N. J. Conway,[2] and J. W. M. Vernimmen[3]
[1)] *Centre for Advanced Instrumentation, Department of Physics, Durham University, Durham, DH1 3LE, UK*
[2)] *Culham Centre for Fusion Energy, Culham Science Centre, Abingdon, Oxon, OX14 3DB, UK*
[3)] *DIFFER - Dutch Institute for Fundamental Energy Research, De Zaale 20, 5612 AJ Eindhoven, the Netherlands*

(Dated: 7 December 2020)

In this paper, the pixelated phase mask (PPM) method of interferometry is applied to coherence imaging (CI) — a family of passive, narrowband spectro-polarimetric imaging techniques for diagnosing plasmas. Compared to designs using a linear phase mask, PPM is more compact, rugged and has a higher spatial resolution (averaged across both image dimensions). A single-delay instrument design is introduced as well as a multi-delay design which uses both pixelated and linear phase masks. The designs are demonstrated with measurements of electron density n_e, via the Stark broadening of the H_γ line at 434.0 nm, made on the Magnum-PSI linear plasma experiment. Comparison of the Abel-inverted multi-delay CI results with Thomson scattering measurements shows good agreement across the $5 \times 10^{19} < n_\mathrm{e} < 8 \times 10^{20}\,\mathrm{m}^{-3}$ range. The neutral temperature estimates of ≈ 3 eV simultaneously inferred from this CI data matches previous spectroscopic studies. For the single-delay CI results, Doppler broadening causes systematic error for $n_\mathrm{e} \lesssim 10^{20}\,\mathrm{m}^{-3}$.

I. INTRODUCTION

Producing steady-state fusion power in the core of a magnetically confined plasma while keeping the power load to the divertor target below the erosion limit is known as the ‘heat exhaust problem’[1]. Solutions to this problem will likely include maintaining the divertor in a detached state and with an optimized geometry. When it begins operations, the MAST-U spherical tokamak will test a range of novel divertor geometries, aided by a suite of diagnostic tools that are "designed for as high space and time resolution as is currently feasible"[2].

One of these tools is coherence imaging (CI) — a narrowband spectral imaging technique that provides 2-D measurements of the lower-order moments of an isolated spectral feature (i.e. the brightness, shift and width)[3,4]. By encoding this information in a set of interference fringes produced at the sensor of a camera, CI can achieve better coverage and higher spatial resolution than is practical for grating spectrometers. Many CI designs are also ‘snapshot’ in that they modulate the interferometer delay spatially across the sensor, so the time resolution is limited only by the camera frame rate or available photon flux. Two CI instruments are planned for MAST-U, one standalone and the other occupying a channel in the multi-wavelength imaging (MWI) system, based on the MANTIS design[5]. One CI application of interest on MAST-U is the measurement of impurity ion flow velocity in the plasma edge, which is well established[6–11]. A second application of interest has received less attention: the measurement of electron density n_e in the divertor via Stark broadening of hydrogen Balmer emission. While this application is established for grating spectrometers[12–16], for CI it has been demonstrated at the proof-of-concept level only[17].

In this work we present CI measurements of n_e made on the Magnum-PSI linear plasma experiment[18] in plasma conditions relevant to the study of divertor detachment ($n_\mathrm{e} \sim 10^{20}\,\mathrm{m}^{-3}$ and temperature $T_\mathrm{e} \sim 1$ eV). We make use of state-of-the-art lineshape calculations in the data analysis and benchmark our results using Thomson scattering measurements. The main novelty of this work is the introduction of new CI instrument designs which incorporate a pixelated micro-polarizer array, generating pixelated fringes that maximize the spatial resolution of the measurement. As well as a more typical single-delay design, we introduce a multi-delay design that sacrifices spatial resolution in exchange for additional spectral information. And we see that, in the case of n_e measurement, this can significantly reduce systematic error due to Doppler broadening.

II. COHERENCE IMAGING WITH A PIXELATED PHASE MASK

Polarized sensors have an array of pixelated polarizers bonded directly to the chip at different orientations. Figure 1 shows the repeating 2×2 polarizer layout of the sensor used in this work. Each 2×2 pixel grid in the image encodes the first three Stokes parameters of the scene, from which the degree of linear polarization and the angle of polarization can be calculated. The use of polarized sensors in interferometry was proposed by Millerd et al.[19] in 2004 with a technique called pixelated phase mask (PPM) interferometry. Compared to a linear phase-mask (LPM), which produces sinusoidal fringes that are roughly straight and parallel (see e.g. Figure 1 in Silburn et al.[7]), the PPM technique has a more compact design and a phase mask that is fixed on manufacture instead of being dependant on the alignment of the optics. The spatial resolution of the two types of phase mask are discussed in Section II A. The PPM technique has been demonstrated for imaging of biological specimens[20,21] and of sound waves[22]. In this section we will consider how PPM interferometry can be used for CI.

[a)] Electronic mail: joseph.allcock@ukaea.uk

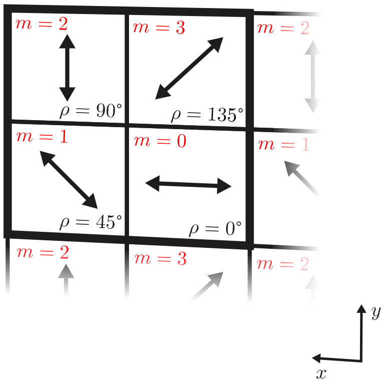

FIG. 1. Pixelated polarizers arranged in the repeating 2×2 grid pattern of the Sony IMX250MZR CMOS sensor used in this work.

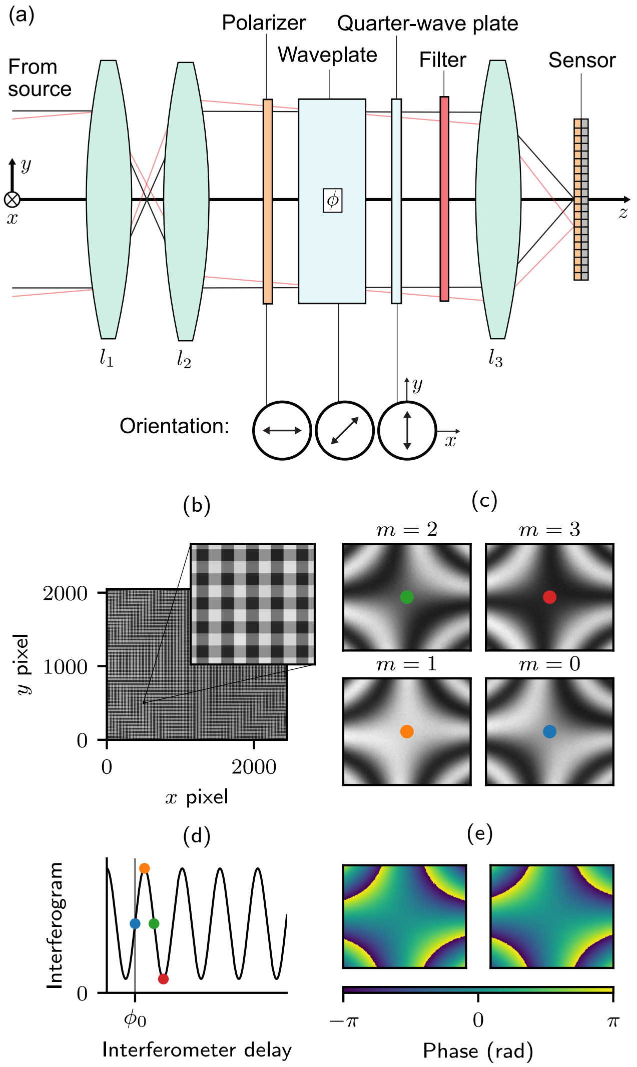

FIG. 2. (a) Optical layout for the single-delay CI configuration. (b) A raw, uniform-brightness calibration image captured by this instrument observing isolated Cd I line emission at 467.8 nm. (c) The four images corresponding to the different orientations of pixelated polarizer, shown separately. (d) The four images correspond to four interferometer delays, with $\frac{\pi}{2}$ rad phase separation. (e) Measured (left) and modeled (right) interferogram phase image for the calibration image in (b).

A. Single-delay configuration

In a simple polarization interferometer, a birefringent waveplate is sandwiched between two linear polarizers, with the waveplate's optic axis making an angle of 45° with the transmission axes of the polarizers[23,24]. The waveplate resolves the light into two equal-amplitude beams in orthogonal polarization states and imparts a phase delay between them. By introducing a quarter-wave plate (QWP) between the waveplate and the final polarizer, with fast axis orthogonal to the front polarizer, the interferometer delay is now determined by the orientation of the final polarizer[19,25]. As such, substituting a polarized sensor for the final polarizer results in as many samples of the interference pattern (over a 2π rad range) as there are unique polarizer orientations. Figure 2(a) shows a schematic of the setup described, with a bandpass optical filter and imaging lens between the QWP and polarized sensor. The three-lens optical layout shown, with an intermediate image plane between l_1 and l_2, is based on the MAST CI system[6,7].

To model the observed interferogram, we use Mueller matrices and Stokes vectors[26]. Let $\mathrm{M_P}(\rho)$ be the Mueller matrix for a polarizer whose transmission axis makes an angle ρ with the x-axis. Let $\mathrm{M_{QWP}}(\rho)$ and $\mathrm{M_{LR}}(\rho,\phi)$ be the Mueller matrices for a QWP and general linear retarder respectively, whose fast axes make an angle ρ with the x-axis. The phase delay imparted by the waveplate ϕ has an implicit dependence on the light's frequency ν. See Appendix A for explicit matrix definitions. The total Mueller matrix for the system described is:

$$\mathrm{M_{SD}} \equiv \mathrm{M_P}\left(m\tfrac{\pi}{4}\right)\mathrm{M_{QWP}}\left(\tfrac{\pi}{2}\right)\mathrm{M_{LR}}\left(\tfrac{\pi}{4},\phi\right)\mathrm{M_P}(0). \qquad (1)$$

To represent the polarized sensor, the orientation of the final polarizer is written in terms of pixel number m, with reference to Figure 1. The Stokes vector representing incident, unpolarized light can be written $\mathrm{S}(\nu)=(I(\nu),0,0,0)$ where $I(\nu)$ is the total spectral radiance. The Stokes vector representing light reaching the sensor is then

$$\mathrm{S}'(\nu)=\begin{pmatrix} I'(\nu)\\ Q'(\nu)\\ U'(\nu)\\ V'(\nu)\end{pmatrix}=\mathrm{M_{SD}}(\nu)\mathrm{S}(\nu), \qquad (2)$$

where the ν-dependence of the Mueller matrix has now been made explicit. The radiance at the sensor is $I'\equiv\int_{-\infty}^{\infty}I'(\nu)d\nu$, which can be evaluated to give:

$$I'=\frac{I}{4}\left(1+\Re\left\{\gamma\left(\phi_0+m\tfrac{\pi}{2}\right)\right\}\right), \qquad (3)$$

where we have also defined $I\equiv\int_{-\infty}^{\infty}I(\nu)d\nu$. Here, $\gamma(\phi_0)$ is the complex degree of temporal coherence. It is a function of the phase delay ϕ_0 between the two interferometer beams at frequency ν_0, corresponding to the center-of-mass frequency of the observed (narrowband) spectrum. The Wiener-Khinchin theorem relates $\gamma(\phi_0)$ to the area-normalized spectral distribution $g(\nu)\equiv I(\nu)/I$ by Fourier transform[24], which can be written as:

$$\gamma(\phi_0)\approx\int_{-\infty}^{\infty}g(\nu)\exp\left(i\phi_0\left[1+\kappa_0\left(\tfrac{\nu-\nu_0}{\nu_0}\right)\right]\right)d\nu. \qquad (4)$$

Here, κ_0 is a dimensionless parameter of order 1 that provides a first-order approximation of the instrument dispersion[4,27].

From Equation 3 we can see that each 2×2 pixel array samples γ at $\frac{\pi}{2}$ rad intervals, encoding information about $g(\nu)$ in a pixelated interference pattern. In CI, ϕ_0 is chosen so as to maximise sensitivity to the plasma parameter of interest.

The hardware used in this work is a modified version of the MAST CI system[6,7]. The camera used is the FLIR Blackfly S, which incorporates the 2448×2048 polarized CMOS sensor shown in Figure 1. The pixel dimension is $3.45\,\mu$m and the camera has a maximum frame rate of 75 Hz. The three DSLR lenses (l_1, l_2 and l_3, see Figure 2(a)) used in this section, have focal lengths 70 mm, 105 mm and 150 mm respectively. The three waveplates available for use in this work are made from alpha barium borate (α-BBO) and have measured thicknesses $L_{\mathrm{WP}} = 4.48$ mm, 6.35 mm and 9.79 mm, each value ± 0.02 mm. The QWP used is a polymer film. All interferometer components are mounted inside a custom temperature-stabilised cell with a nominal regulation accuracy of ±0.25°C. A uniform-brightness test image was obtained with the CI instrument in this configuration, with a Cd gas-discharge lamp illuminating an integrating sphere as the source. The Cd I line at 467.8 nm was isolated using a bandpass filter. For demonstration purposes, the three available waveplates were used at once, their axes aligned so as to combine the phase delays constructively. The raw measured image is shown in Figure 2(b). In Figure 2(c) the four interleaved images corresponding to the four polarizer orientations are shown separately. The hyperbolic fringe pattern is caused by the dependence of ϕ_0 on ray angle through the waveplate[28] and the $\frac{\pi}{2}$ rad phase shift between images with consecutive m-number is clearly visible.

Interferogram contrast $\zeta \equiv |\gamma|$ and phase $\Phi \equiv \arg\gamma$ are related to the observed spectrum $g(\nu)$ by Equation 4. Different PPM demodulation algorithms have been suggested[19,29,30] for recovering ζ and Φ, but in this work we use the simple 'four-bucket' demodulation algorithm for the single-delay CI data[19]. Figure 2(e) shows a good match between the demodulated calibration image Φ (left) and the corresponding modeled Φ (right). This model uses the equation for phase delay due to a uniaxial plane-parallel crystal plate[28] and sets Φ to zero at the image center, since the model parameter values are not sufficiently accurate to recover absolute Φ.

In LPM CI, the necessary phase shear across the image is typically created using either a 'displacer plate'[9,10,31] or a waveplate and Savart plate in combination[6,7,11]. A displacer plate is a single birefringent plate with an intermediate cut angle and a Savart plate is a composite of two displacer plates, aligned so as to produce the shear while imparting zero net delay for on-axis rays[23,24]. The PPM system described is more compact than either LPM system, requiring fewer birefringent plates than the Savart design and requiring a thinner birefringent plate than the displacer design (for an equivalent on-axis delay).

The spatial resolution at which the ζ and Φ images are recovered from an LPM interferogram is anisotropic. Perpendicular to the phase shear the pixel width sets the spatial resolution (we are assuming detector-limited operation). Parallel to the phase shear, it depends on the width of the Fourier-domain filter used in the demodulation process. Modelling done in previous work[6] of MAST CI images suggests 2 fringe periods as the approximate width of the Φ point spread function in this direction. In CI, the LPM fringe period is typically chosen to be > 6 pixels, so as to avoid contrast degradation due to phase shear across the pixel area. The PPM spatial resolution is 2 pixels or better in both dimensions, depending on the demodulation algorithm used[29]. When averaged over both dimensions, the spatial resolution possible using a PPM is likely to be considerably higher than when using an LPM. See Section V for related discussion.

B. Multi-delay configuration

Plasma line spectra are often complicated by the presence of multiple components and broadening mechanisms. In these cases, encoding γ at multiple interferometer delays can make interpretation easier and reduce systematic error. For example, Michael et al.[27] used CI to characterize the neutral velocity distribution function in an argon plasma via the Doppler-broadened lineshape. But that work used a single-delay CI design, with samples of γ built up at different delays by observing repeated plasma discharges with different waveplate thicknesses. More recent work[32] made measurements of charge exchange recombination emission using a snapshot multi-delay CI design, but interpretation of the results was inconclusive.

The single-delay CI system from the previous section can be turned into a multi-delay system by introducing a polarizer, waveplate and Savart plate to the front of the interferometer, with order and orientations shown in Figure 3(a). The Mueller matrix for this configuration can be written:

$$\mathrm{M}_{\mathrm{MD}} \equiv \mathrm{M}_{\mathrm{SD}}\mathrm{M}_{\mathrm{LR}}\left(\tfrac{\pi}{4}, \psi\right)\mathrm{M}_{\mathrm{P}}(0). \tag{5}$$

Where M_{SD} was defined in Equation 1 and where ψ is the delay imparted by the waveplate and Savart plate in combination, with implicit dependence on frequency and sensor plane position. Instead of this waveplate-Savart plate combination, a displacer plate could be used. To find an expression for the radiance at the sensor plane I' under observation of unpolarized light we proceed as in the case of the single-delay configuration by evaluating $\int_{-\infty}^{\infty} \mathrm{M}_{\mathrm{MD}}(\nu)\mathrm{S}(\nu)d\nu$. It can be shown that this gives:

$$\begin{aligned} I' = \frac{I}{8}\Big(1 &+ \Re\{\gamma(\psi_0)\} \\ &+ \Re\{\gamma(\phi_0 + m\tfrac{\pi}{2})\} \\ &+ \frac{1}{2}\Re\{\gamma(\phi_0 + \psi_0 + m\tfrac{\pi}{2})\} \\ &+ \frac{1}{2}\Re\{\gamma(\phi_0 - \psi_0 + m\tfrac{\pi}{2})\}\Big). \end{aligned} \tag{6}$$

Here, ψ_0 is the phase delay imparted by the waveplate and Savart plate in combination at frequency ν_0.

From Equation 6 we can see that this interferogram encodes γ at four fixed delays: ϕ_0, ψ_0, $\phi_0 + \psi_0$ and $\phi_0 - \psi_0$. These delays arise as follows. The light exiting the second polarizer in the system is the sum of two beams with with relative delay ψ_0 between them. The second waveplate then splits each of these beams again into a pair of orthogonally polarized beams and introduces a further delay ϕ_0 between each pair. When the four beams interfere at the sensor, γ is encoded at the relative delay for each possible beam pair. The combination of PPM and LPM terms can be seen in the measured image shown raw in Figure 3(b) and zoomed in Figure 3(c), which observes the same Cd lamp setup as the single-delay CI image in Figure 2(b). The Savart plates available for use in this work

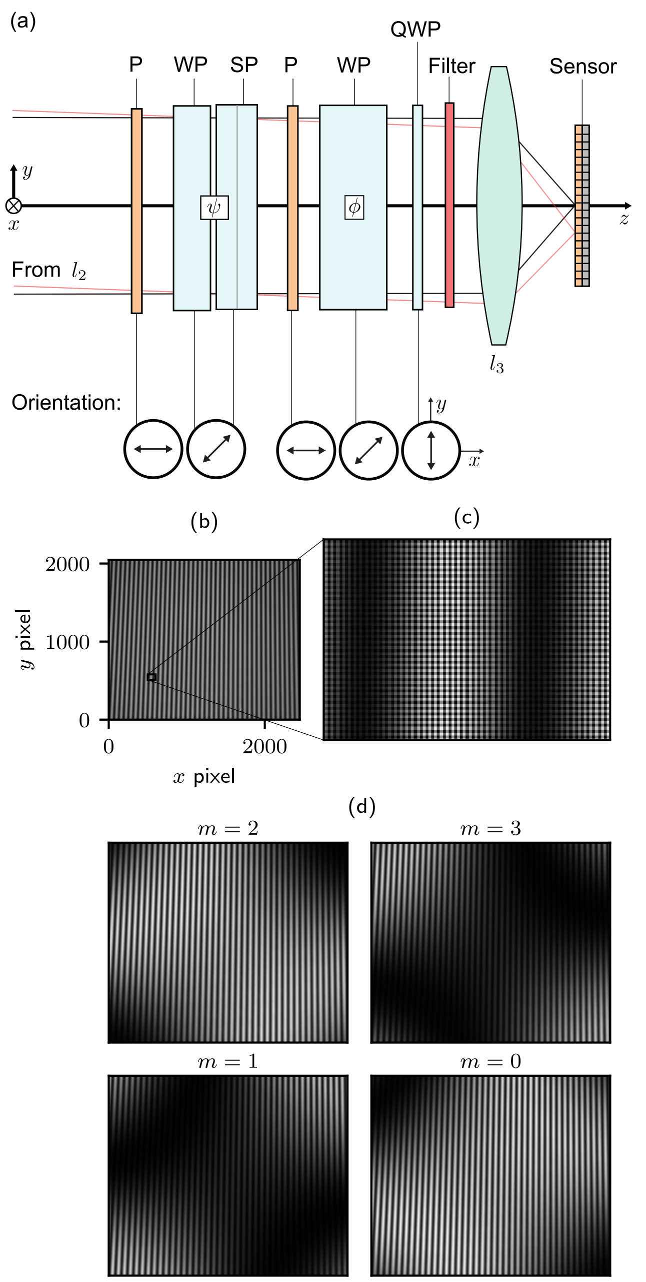

FIG. 3. (a) Optical layout for multi-delay coherence imaging. The system's front two lenses, l_1 and l_2, are not shown here. The shorthand labels here refer to polarizer (P), waveplate (WP), Savart plate (SP) and quarter-wave plate (QWP). (b) A raw, uniform-brightness calibration image captured by this instrument observing isolated Cd I line emission at 467.8 nm. (c) Zoomed view of (b). (d) The four images corresponding to the different orientations of pixelated polarizer, shown separately.

	Single-delay	Multi-delay 1	Multi-delay 2
$L_{\mathrm{WP}} : \phi$ (mm)	4.48	6.35	4.48
$L_{\mathrm{WP}} : \psi$ (mm)	-	4.48	9.79
L_{SP} (mm)	-	$4+2.2$	$4+2.2$
ϕ_0 (10^3 rad)	8.19 ± 0.06	11.8 ± 0.1	8.19 ± 0.06
ψ_0 (10^3 rad)	-	8.19 ± 0.06	18.4 ± 0.1
$\phi_0 + \psi_0$ (10^3 rad)	-	20.0 ± 0.1	26.6 ± 0.1
$\phi_0 - \psi_0$ (10^3 rad)	-	3.6 ± 0.1	10.2 ± 0.1
$\zeta_{\mathrm{I}}(\phi_0)$	0.813 ± 0.003	0.78 ± 0.02	0.81 ± 0.01
$\zeta_{\mathrm{I}}(\psi_0)$	-	0.58 ± 0.02	0.66 ± 0.01
$\zeta_{\mathrm{I}}(\phi_0 + \psi_0)$	-	0.54 ± 0.02	0.64 ± 0.02
$\zeta_{\mathrm{I}}(\phi_0 - \psi_0)$	-	0.56 ± 0.02	0.62 ± 0.01

TABLE I. Setup and calibration information for the three CI configurations used in Section IV of this work. L_{WP} and L_{SP} are waveplate and Savart plate thicknesses, respectively. Interferometer delays correspond to normal ray incidence and wavelength $\lambda_0 = 434.0$ nm, see text for details of their measurement. The values for the instrument contrast ζ_{I} calibration factor correspond to the image center of measurements of the Cd I line at 467.8 nm. Each value is the averaged of ~ 10 measurements taken throughout the day and the quoted uncertainty is the corresponding standard deviation.

are α-BBO and have thicknesses $L_{\mathrm{SP}} = 4$ mm and 2.2 mm. In all results shown here, these plates are aligned so as to function as a single plate of thickness $L_{\mathrm{SP}} = 6.2$ mm. For the system described, this gives a fringe period of ~ 55 pixels at $\lambda = 434.0$ nm, far from optimal in terms of spatial resolution but usable for testing. The waveplates in the ψ_0 and ϕ_0 positions in Figure 3(a) have $L_{\mathrm{WP}} = 4.48$ mm and $L_{\mathrm{WP}} = 6.35$ mm respectively, we call this configuration 'Multi-delay 1' (see Table I for reference). In Figure 3(c) four interleaved images corresponding to the four polarizer orientations are shown separately.

Demodulation of the multi-delay interferogram to obtain ζ and Φ images for each of the four delays is more involved than in the single-delay case. First, it is noted that the PPM has its spatial carrier frequencies at the x and y Nyquist frequencies (see e.g. Figure 2 in Kimbrough & Millerd[29]). This is sufficiently well separated in frequency space from the LPM term $\gamma(\psi_0)$ that $\zeta(\psi_0)$ and $\Phi(\psi_0)$ can be extracted using established Fourier-domain filtering techniques[33]. To demodulate the three remaining terms we use 'synchronous demodulation'[30], which involves multiplying the interferogram by a reference image that is the PPM in complex exponential form: $\exp(im\frac{\pi}{2})$. By the Fourier transform shifting property, in frequency space the $\gamma(\phi_0 + m\frac{\pi}{2})$ term is now shifted from the x and y Nyquist frequencies down to the zero frequency. Additionally, the $\gamma(\phi_0 \pm \psi_0 + m\frac{\pi}{2})$ terms are now shifted to the $\pm\psi_0$ spatial frequencies. All three remaining terms can now be demodulated using Fourier-domain filtering techniques[33].

To interpret the measured ζ and Φ values, the interferometer delay at λ_0 must be known. This calibration step has already been carried out in previous work[6,7] for the three α-BBO waveplates used. Table I lists the interferometer delays for the three CI instrument configurations used in the remainder of this work for $\lambda_0 = 434.0$ nm. The quoted uncertainty on these values accounts for both measurement error and estimated uncertainty in the α-BBO dispersion model used to convert to the relevant wavelength for this work. This delay uncertainty is not accounted for in the analysis presented here.

In the next section, we will look at how single-delay and multi-delay CI systems can be used to measure snapshot 2-D images of plasma electron density n_{e}.

III. COHERENCE IMAGING MEASUREMENT OF ELECTRON DENSITY

A. Modelling Balmer series lineshapes

In divertor conditions the hydrogen Balmer series lineshapes are determined by Stark broadening, Doppler broadening and Zeeman splitting[12,14]. Since CI can only target a single line, line choice for n_e measurement is a trade-off: the further up the Balmer series (i.e. the higher the principal quantum number of the initial state), the larger the Stark width but the lower the brightness[16]. Practical issues can also be important like nearby impurity lines that can contaminate the measurement. In this work we consider H_γ ($5 \rightarrow 2$, $\lambda_0 = 434.0\,$nm) only.

In previous CI work[17], the Stark-broadened H_γ lineshape was approximated using a Lorentzian function with width $\propto n_e^{2/3}$. In this work we instead use a table of Stark-Zeeman lineshapes, generated for plasma diagnostic applications by Rosato et al.[34] by numerical solution of the Schrödinger equation. This model takes as its inputs n_e, magnetic field strength $\boldsymbol{B}$ and also plasma temperature T — upon which the Stark profile has only a weak dependence. This model assumes pure deuterium, but the result for pure hydrogen can be approximated by multiplying the input temperature by 2 (effectively dividing the ion mass by 2 in the calculation of ion thermal velocity)[35]. For the Doppler broadening contribution we assume a Gaussian profile throughout this work i.e. a Maxwellian velocity distribution for the emitting species, at temperature T_n. This assumption is justified in the context of Magnum-PSI in Section IV B. The relative strengths and polarization states of the observed Zeeman-split π and σ line components are determined by the angle between $\boldsymbol{B}$ and the line of sight[36]. In similar work, Zeeman splitting is either ignored[13–15,17] or accounted for using knowledge of the B-field[12], depending on $|\boldsymbol{B}|$, the line being measured and the view geometry. For a transverse view of the field, a polarizer with the appropriate orientation can be used to completely suppress the σ components, leaving only the central π component[37].

In Figure 4(a), this model is used to plot the H_γ lineshape for three different values of n_e, with $T_e = T_n = 1\,$eV. The corresponding Lorentzian approximations (with the same Doppler broadening assumption) are also plotted. The Rosato et al. model has $|\boldsymbol{B}| = 1\,$T but the σ line components are suppressed for a more direct comparison of the Stark contribution. For each of the lineshapes, Figure 4(b) plots the corresponding ζ profile as a function of interferometer delay, calculated using Equation 4. It is clear that the Lorentzian approximation can lead to a large underestimate of the n_e value inferred from ζ, so it is not considered any further here. The four vertical lines in Figure 4(b) correspond to the four delays of the multi-delay 1 CI setup.

Since independent lineshape broadening / splitting contributions are combined by convolution, the corresponding contributions to γ (and so too to ζ) are combined by multiplication (by the convolution theorem). Figure 4(b) plots estimates of ζ_Z, the multiplicative contribution due to Zeeman splitting, for $|\boldsymbol{B}| = 1\,$T for both a transverse ($\perp$) view and a longitudinal ($\parallel$) view of the field. These are calculated using the Rosato et al. model by dividing ζ profiles with $|\boldsymbol{B}| = 1\,$T by ζ with $|\boldsymbol{B}| = 0\,$T. It was found that they match the ζ_Z predicted by a simple 'strong-field' Zeeman approximation[36] to within 1% for the parameters shown. The gray shaded region indicates the full range of values ζ_Z ($\perp$ view) can take for $|\boldsymbol{B}| = 1\,$T, depending on the relative orientation of the front CI polarizer and $\boldsymbol{B}$. These profiles show that the ζ_Z contribution can be significant for low n_e and large delay, and that the orientation of the CI front polarizer needs to be considered.

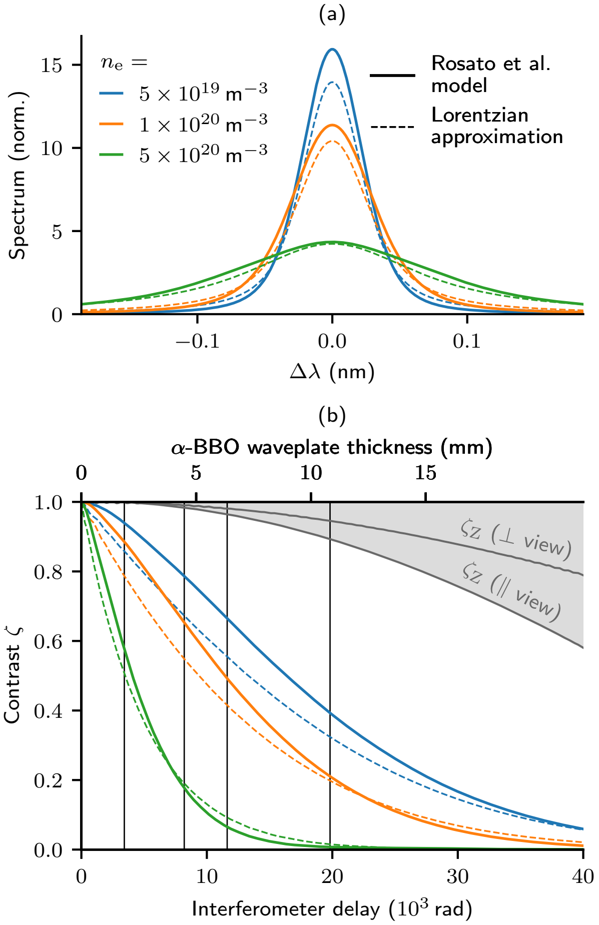

FIG. 4. (a) Modeled lineshapes for H_γ emission at 434.0 nm over a range of n_e for $T_e = T_n = 1\,$eV and $|\boldsymbol{B}| = 1\,$T (Zeeman σ components suppressed). The two line styles correspond to the different lineshape models. (b) The corresponding modeled ζ profiles as a function of interferometer delay.

If $g(\nu)$ is symmetric about ν_0 then, by Equation 4, it's distribution can be fully reconstructed from the ζ profile — the Φ profile encodes the line center ν_0 only. For a homogeneous emitter, the lineshape model described above is symmetric about ν_0, and the analysis methods introduced in the next section will consider ζ only. However, an observed $g(\nu)$ that is line-integrated through an inhomogeneous emitter will not, in general, be symmetric due to Doppler shifts. Inversion of line-integrated results in the context of Magnum-PSI will be discussed in Section IV B.

B. Fitting to measured CI contrast

Inferring n_e from measurements of ζ made at one or more delays is a curve-fitting problem, requiring fast evaluation of the modeled ζ. To do this we have pre-calculated a lookup table (LUT) for ζ on a grid spanning the expected range of n_e, $T_e = T_n$, $\boldsymbol{B}$ and interferometer delay. LUT interpolation then allows for fast comparison to the data for fit optimization. For the curve-fitting framework, we use Bayesian parameter estimation. When fitting, we will assume that $\boldsymbol{B}$ and interferometer delay is known perfectly well and also that $T_e = T_n$. This leaves n_e and T_n as the free model parameters to be optimized.

For a single-delay CI measurement of ζ, the most that can be inferred about n_e without making assumptions about T_n is an upper limit. While similar work[17] assumed Doppler broadening to be negligible, we will make the more conservative assumption of a 6 eV (soft) upper limit on T_n, using the prior probability density function (PDF):

$$P(T_n) \propto \frac{1}{1+\exp(k[T_n - 6\,\mathrm{eV}])}, \tag{7}$$

where we choose $k = 4\,\mathrm{eV}^{-1}$. This prior PDF is only necessary for the single-delay CI data. The likelihood function for each ζ data point is assumed to be a normal distribution and noise on the measurements made at different delays and at different points in the image is assumed to be uncorrelated. The product of the prior PDF and total likelihood function at each image point is proportional to the posterior PDF, which can be evaluated on the LUT parameter grid to find the the maximum a posteriori probability (MAP) estimate for parameters n_e and T_n. Marginal posterior PDFs for n_e and T_n and confidence intervals are calculated using a Markov chain Monte Carlo (MCMC) method[38].

In testing this LUT-based ζ-fitting tool on modeled spectra, we can quantify the systematic error due to Doppler broadening — particularly important in the case of single-delay CI. To do this, ζ profiles are generated over a range of n_e and $T_e = T_n$. Zero-mean Gaussian noise is added to the modeled ζ, with realistic standard deviation $\sigma_\zeta = 0.02$. Then, ζ is fit to and the n_e MAP determined. For each set of inputs, the average n_e MAP is taken over 100 independent instances of the measurement noise. This procedure is carried out first for the single-delay CI configuration from Table I, and the results are plotted in Figure 5(a). This shows that the overestimate in n_e can be significant even for moderate T_n — e.g. $> 25\%$ at $n_e = 7\times10^{19}\,\mathrm{m}^3$ and $T_n = 3$ eV — and becomes very large for low n_e and moderate T_n. Figure 5(b) then plots the same test, but for the multi-delay 1 CI configuration from Table I. This shows a significant reduction in systematic error, extending the range over which n_e can be inferred with accuracy down to lower n_e and/or higher T_n conditions. In the next Section, the new CI methods introduced are tested experimentally.

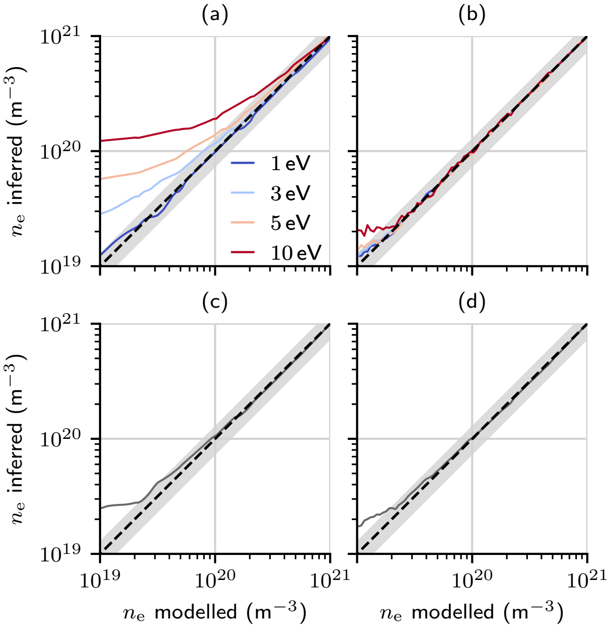

FIG. 5. Predicted error in inferred n_e due to Doppler broadening as a function of modeled n_e, where the gray shaded region indicates ±25% error. (a) and (b): Gaussian Doppler broadening plotted across a range of T_n for (a) the single-delay CI configuration and (b) the multi-delay 1 configuration (see Table I). (c) and (d): non-Gaussian Doppler broadening caused by two emitting hydrogen populations with different temperatures (3 eV and 0.3 eV) and intensity ratio 2:1. Shown for (c) single-delay and (d) multi-delay CI.

IV. EXPERIMENTAL TESTING ON MAGNUM-PSI

A. Setup and operation

Magnum-PSI is a linear plasma experiment capable of producing steady-state plasma beams with temperatures (0.1 – 5 eV), densities (10^{19} – $10^{21}\,\mathrm{m}^{-3}$) and field strengths (0 – 2.5 T), matching the divertor conditions of current and future tokamaks[18]. A cascaded arc source produces a plasma beam of diameter ∼ 20 mm that is confined by the field of five superconducting solenoid magnets. A movable, replaceable target sits 1.5 m downstream from the source, within a vacuum vessel of diameter 0.5 m. The control parameters for Magnum-PSI are the source gas flow Q_s in standard liters per minute (SLM), source current I_s and $|\boldsymbol{B}|$. In this section, we use the CI techniques described above to measure the n_e profile of the Magnum-PSI beam for a range of plasma conditions, benchmarking our results against the Thomson scattering (TS) diagnostic system[39], whose reported n_e measurement accuracy is better than 5%.

The CI instrument was mounted on the railing of a mezzanine area, a distance of 5.5 m from the Magnum-PSI beam axis. Figure 6(a) shows a photo of the installed CI setup in relation to the experiment. A telephoto DSLR lens with focal length 600 mm and $f/6.3$ occupies the l_1 position, while l_2 and l_3 have focal lengths 105 mm and 150 mm respectively (see Figure 2(a)). This provides a vertical field of view of 0.5°, appropriate for imaging the beam through a 70 mm diameter port in the vacuum vessel. This port views the beam a few cm from the target, at the same position along the beam's axis as the vertical TS laser path and also the view of a grating spectrometer. Figure 6(b) shows this geometry as viewed from the source. Figure 6(c) shows the measured transmission profile of the two-cavity interference filter used in the CI system to isolate the H_γ emission. Also shown is the line spectrum measured by the Magnum-PSI spectrometer looking through the beam axis.

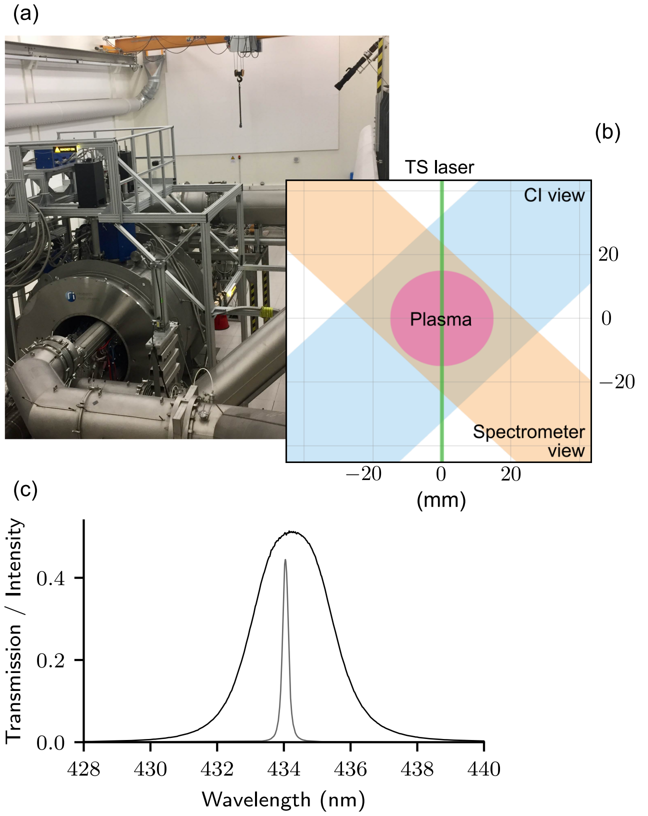

FIG. 6. (a) The Magnum-PSI experiment hall. The CI instrument can be seen in the top-right corner. (b) The CI and spectrometer views relative to the TS laser path and the plasma beam, as viewed from the plasma source.

The CI camera was connected to a PC on the mezzanine and its settings were remotely controlled from the experiment control room. Before the start of operations, the CI temperature controller was set to 35 ± 0.25°C and left for 2 hours to equilibrate.

Calibration of the CI instrument contrast factor ζ_I is analogous to calibration of the instrument function of a grating spectrometer[3]. ζ_I was measured using a Cd lamp illuminating an integrating sphere, roughly every hour during operations. The system was unmounted and calibration images like those shown in Figures 3(b) and 3(b) were captured of the Cd I line at 467.8 nm, the appropriate filter having been swapped in. Table I lists the measured ζ_I for each instrument and each delay, averaged over the central 20×20 pixel region. No clear trend was observed in ζ_I throughout operations so the quoted values are averages over all images collected by that instrument and the quoted uncertainty is the corresponding standard deviation. It is worth noting that ζ_I for the pure PPM term ($\zeta_I(\phi_0)$) is significantly better than for the LPM terms. This could be due to the large number of crystals used to encode the LPM, each one having variations in imparted phase delay across its aperture. Another possible cause is increased sensitivity of the LPM terms to temperature variations or mechanical disturbance during mounting. Dark frames were also captured with each ζ_I, and were subtracted from all images before demodulation. We will refer to the contrast extracted from the raw measurements of Magnum-PSI as $\check{\zeta}$ to distinguish it from the Abel-inverted contrast profiles. Each $\check{\zeta}$ image was divided through by the corresponding ζ_I image prior to analysis.

Figure 7(a) shows an example interferogram for the multi-delay 1 CI system viewing the Magnum-PSI beam. This image was exposed for $t_{\text{exp}} = 0.8\,\text{s}$ and details of the plasma control parameters are given in the figure caption. The peak n_e and T_e on-axis reported by the TS diagnostic for this discharge is $n_e = 7.90 \times 10^{20}\,\text{m}^{-3}$ and $T_e = 1.77\,\text{eV}$. Figure 7(b) shows the extracted brightness image and Figure 7(c) shows the extracted (and calibrated) $\check{\zeta}$ images for the four delays. In Figure 7(d), $\check{\zeta}$ is plotted as a function of delay for the image center. Also plotted is the $\check{\zeta}$ profile predicted by substituting the lineshape measured by the grating spectrometer during the same discharge into Equation 4, dividing through by the corresponding $\check{\zeta}$ profile of spectrometer instrument function. The two instruments show good agreement despite viewing the plasma beam along orthogonal view chords.

Since the line-integrated profiles do not show significant variation along the beam axis, for the remainder of this work we will present results from a central column slice through the images.

B. Non-Gaussian Doppler broadening and Doppler shifts

The presence of non-Gaussian Doppler broadening or significant Doppler shifts could complicate the interpretation of the CI data. Previous work by Shumack et al.[37] used a grating spectrometer to view H_β (486.1 nm) at the plasma source of the Pilot-PSI machine (a smaller, non-superconducting forerunner to Magnum-PSI that used the same cascaded arc plasma source). From the observed lineshape, the presence of two atomic hydrogen populations was inferred: one coupled to the ions via charge exchange with T_n at a few eV and the other one cold at 0.1–0.5 eV. The intensity ratio between the two populations was constant across the beam profile at roughly 2 to 1 (hot to cold). In addition, the hot population was observed to be rotating around the beam axis, at velocities up to 10 km/s, due to an $\boldsymbol{E} \times \boldsymbol{B}$ drift. Since this rotation was observed to decrease with axial distance from the source, with a characteristic decay length of 0.5 m, it is not expected in our measurements at the Magnum-PSI target, which sits 1.5 m from the source.

The presence of two emitting populations at different temperatures results in a non-Gaussian Doppler broadening contribution to the lineshape, which could introduce systematic error into the inferred n_e if not accounted for. This size of this error was modeled by the same fitting procedure used in Section III B. Representative T_n chosen for the hot and cold populations in this test are 3 eV and 0.3 eV. Figure 5(c) shows the predicted error for the single-delay CI configuration and Figure 5(d) shows the error for the multi-delay 1 CI configuration. As might be expected, the presence of the cold population actually reduces the error due to Doppler broadening in the single-delay case when compared to the Gaussian broadening model with $T_n = 3\,\text{eV}$. In the case of the multi-delay CI, the error in inferred n_e is only larger than 5% for $n_e < 5 \times 10^{19}\,\text{m}^{-3}$. Since the predicted effect is small, we do not account for the possibility of this type of non-Gaussian Doppler broadening in the interpretation of the Magnum-PSI CI results presented.

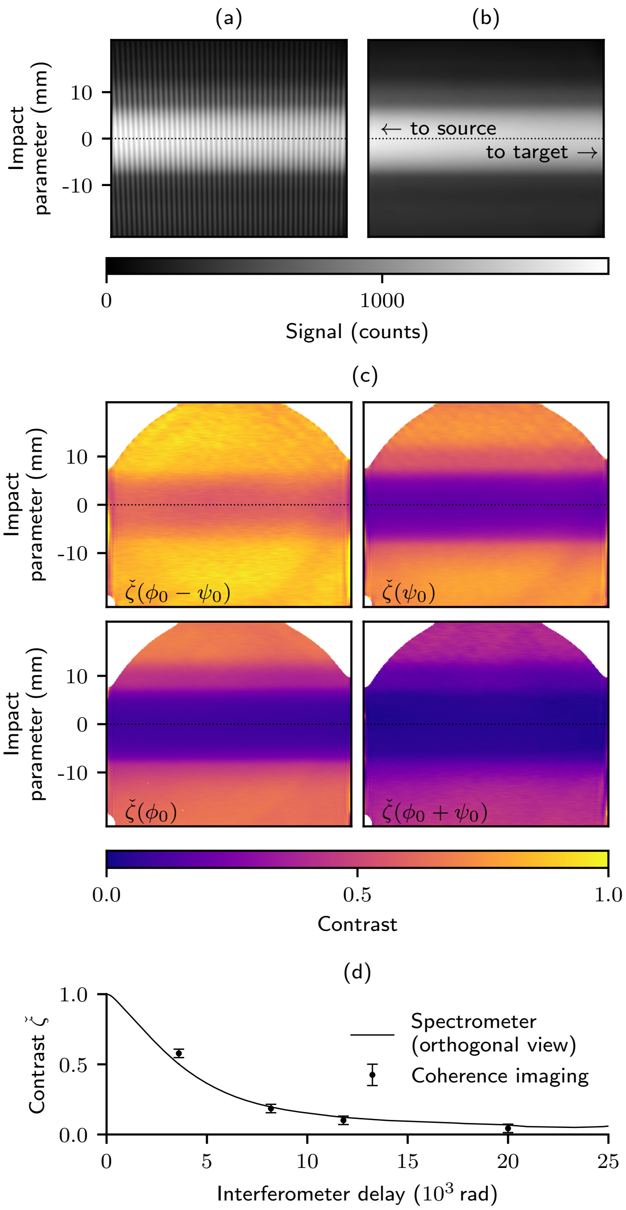

FIG. 7. (a) The raw CI interferogram for an instrument in the multi-delay 1 configuration (see Table I) observing H_γ emission from Magnum-PSI, with control parameters set to $I_s = 200$ A, $|\boldsymbol{B}| = 1.2$ T. Exposure time was 0.8 s (b) The brightness profile extracted from (a). (c) The contrast profiles extracted from (a) after calibration. (d) Contrast plotted as a function of delay for the CI results in (c), viewing through the beam axis at the image center. Also plotted for comparison is the the $\check{\zeta}$ calculated from the grating spectrometer measurements, again viewing through the beam axis but at 90° to the CI view.

C. Abel inversion

The spectrum observed at each pixel has been integrated along a path L through the plasma. It can be shown that, provided the range of Doppler shifts along L is small, the observed contrast $\check{\zeta}(\phi_0)$ is related to the local contrast $\zeta(\phi_0, \boldsymbol{r})$ at point $\boldsymbol{r}$ by:

$$\check{\zeta}(\phi_0) \approx \frac{1}{I}\int_L \varepsilon(\boldsymbol{r})\zeta(\phi_0, \boldsymbol{r})dl. \tag{8}$$

Here, $\varepsilon(\boldsymbol{r})$ is the local emissivity, satisfying:

$$I = \int_L \varepsilon(\boldsymbol{r})dl. \tag{9}$$

Since $\check{\zeta}$ is weighted by $\varepsilon(\boldsymbol{r})$, Equation 9 must be inverted before Equation 8 can be inverted to yield $\zeta(\phi_0, \boldsymbol{r})$. Since the CI sight-lines all view the beam from the same direction, we assume that the plasma has cylindrical symmetry about the central beam axis in order to obtain a unique inversion solution. To make a first-order account for asymmetry, while maintaining a unique solution, we split the line-integrated measurements in to two halves along the beam axis and invert each side separately. This then assumes that we have two half-cylinders, each with its own cylindrical symmetry, joined along the plane containing the beam axis and the lines of sight.

Both the brightness and contrast profiles are Abel-inverted using the simultaneous algebraic reconstruction technique (SART)[40], an iterative technique that has been used in previous CI work[6,7]. Each pixel's line of sight is assumed to be narrow and to have equal collection power along its length. Line-integrated brightness profiles are brought smoothly to zero outside of the image edges prior to inversion. The position of the beam axis on the line-integrated profiles is estimated by choosing the brightest point in the smoothed, line-integrated brightness profile (See the black dotted lines in Figure 7). The radial inversion grid chosen extends to 30 mm and has 300 bins, for a grid resolution of 0.1 mm. For the multi-delay CI results, the $\check{\zeta}$ profile is inverted independently for each of the four delays.

D. Comparison with Thomson Scattering

Once the local ζ profile(s) have been calculated, the fitting procedure described in III B is used to infer n_e. Figures 8(a)–(e) plot the multi-delay CI results for an ascending scan in beam n_e, see the figure caption for the corresponding Magnum-PSI control parameters. Figure 8(e) corresponds to the raw and demodulated images shown in Figure 7. The top row shows 3-D plots of the inverted ζ profiles in black as a function of beam radius and delay. The grey mesh surface represents the MAP values for the fit to the ζ data at each r, plotted over a gridded delay axis. Three slices through this surface are made at radial positions $r = 3, 9$ and 15 mm, plotted in blue, orange and green respectively. In the second row, each of these slices is plotted in as a function of delay only, along with the corresponding four ζ data points, allowing for inspection of the goodness of fit. The third row then plots the radial n_e profiles as inferred from the CI and TS. For the CI results, the MAP values are plotted as a solid line and the 68% confidence interval is shaded. The r values of the three slices are indicated with vertical lines. Finally, the fourth row plots the corresponding radial T profiles: T_e for the TS and T_n for CI. For the CI data, only the 68% confidence interval is shown, as the inferred posterior PDFs are relatively wide.

The agreement between the ζ data and the fit profiles looks good for these measurements, particularly closer to the beam

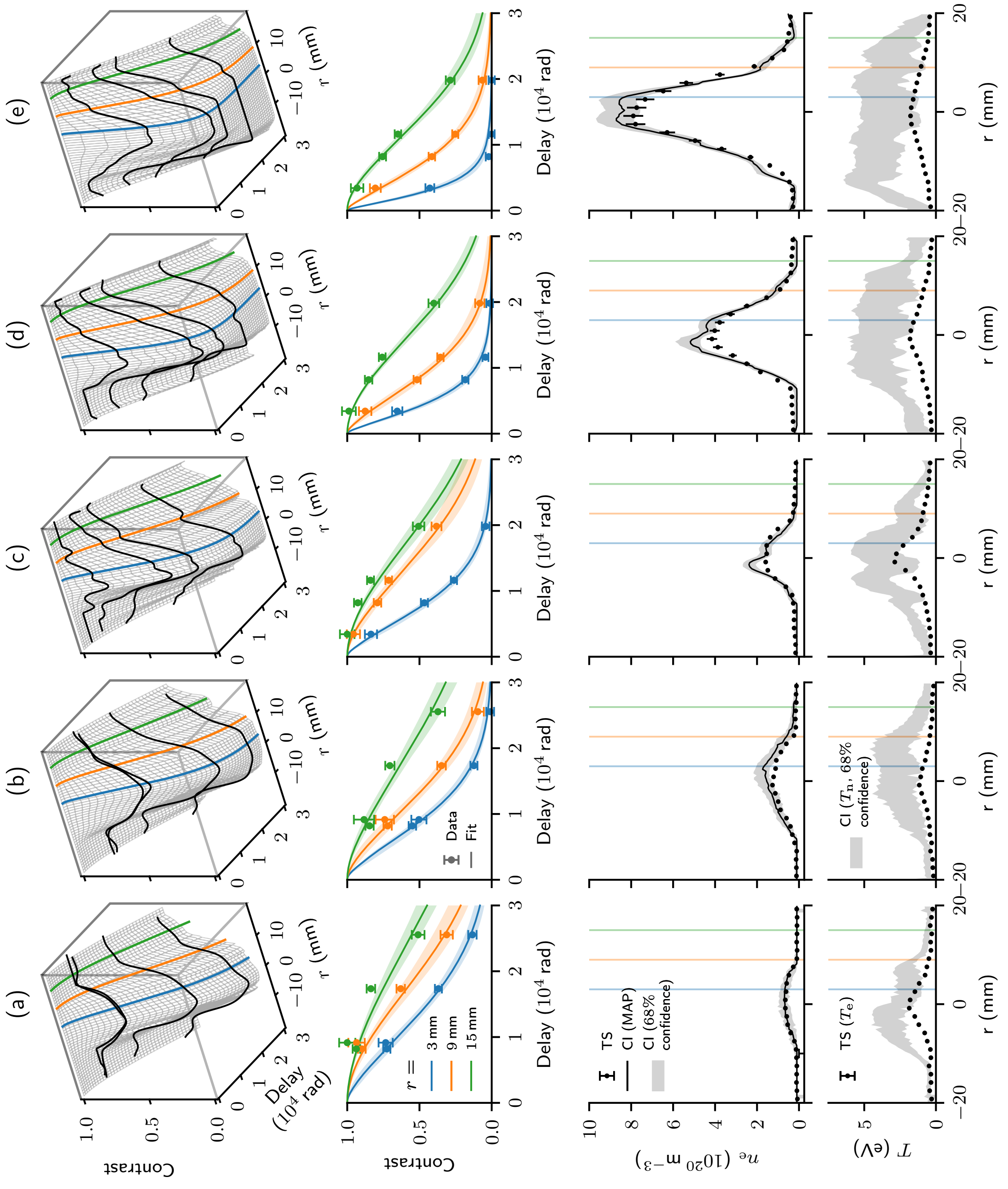

FIG. 8. Inverted multi-delay CI results where columns (a)–(e) correspond to a scan from low to high n_e on Magnum-PSI. In the top row, inverted ζ profiles are plotted in black vs. interferometer delay and beam radial coordinate r. The mesh surface is the best fit to this data. The second row plots slices at three different r values indicated by color, showing both CI data and fit. The third row then compares the n_e profiles reported by CI and Thomson scattering. The final row compares the emitter temperature T_n inferred from the CI data to the measured TS T_e profiles. Source gas flow rate is $Q_s = 5$ SLM for all discharges here, while source current I_s and $|\boldsymbol{B}|$ are: (a) $I_s = 120$ A, $|B| = 0.8$ T, (b) $I_s = 130$ A, $|B| = 0.8$ T, (c) $I_s = 125$ A, $|B| = 1.2$ T, (d) $I_s = 160$ A, $|B| = 1.2$ T, (e) $I_s = 200$ A, $|B| = 1.2$ T.

axis. Agreement between CI and TS n_e profiles is mostly good across this range. It is important to note that the results in Figures 8(a) and (b) were taken with the CI instrument in the multi-delay 2 configuration while the results in Figures 8(c)–(e) were taken with the multi-delay 1 configuration. The larger maximum delay of the multi-delay 2 configuration ought to make it more sensitive at lower n_e. While the multi-delay 2 configuration does provide four fixed interferometer delays, two of these delays are similar in value, representing a sub-optimal sampling. However, the close proximity of the samples provides a welcome consistency check. The T_n inferred from the CI data is consistently higher than the T_e reported by the TS, consistent with previous spectroscopic measurements on Pilot-PSI[37].

Figure 9 plots inverted single-delay CI results from Magnum-PSI, presented in the same format as Figure 8. Results correspond to another low-to-high scan in n_e at a higher field of $|\boldsymbol{B}|$. See figure caption for full details of the

Magnum-PSI control parameters. While the n_e profile inferred from single-delay CI shows good agreement with the TS for $n_\mathrm{e} > 10^{20}$ m^3, Figure 9(a) shows that at lower densities ($n_\mathrm{e} \approx 5 \times 10^{19}$ m3) we see a considerable ($\sim 200\%$) overestimate in the CI n_e. Based on the modeling in Section III B, we expect a degree of n_e overestimation for the single-delay instrument. However, the observed overestimation is larger than we would expect by taking the TS n_e and T_e and calculating the expected overestimation.

V. DISCUSSION

Although the simple plasma geometry of Magnum-PSI aids comparison between spectroscopy and Thomson scattering diagnostics, it does not fully demonstrate the advantages of the PPM CI method over the LPM method. To simulate CI images for a realistic MAST-U divertor view, we have used the the CHERAB spectroscopy modeling framework[41,42]. For the plasma profiles we have used existing SOLPS modeling for MAST-U core scope plasma presented elsewhere[43]. The Stark-broadened H_γ narrowband spectral image modeled by CHERAB is used to generate a CI interferogram with delay depending on the instrument configuration chosen. Figure 10 shows synthetic CI images viewing H_γ emission from the MAST-U divertor. Modeled spectra can then be used to calculate the observed CI interferogram as in Section II. Figure 10(a) shows a CI image with an LPM whose fringe period is roughly 10 pixels, produced using a displacer plate CI system. Figure 10(b) then shows a CI image with a PPM, produced using the single-delay design introduced in Section II A. Both systems have an on-axis phase delay of 8000 rad. Figures 10(c) and Figures 10(d) then show the demodulated (and calibrated) $\check{\zeta}$ images for the LPM and PPM interferograms respectively. In the zoomed view of the LPM $\check{\zeta}$, ringing artefacts are visible around regions of the background brightness image with high spatial frequency, caused by imperfect separation in image frequency space between the background brightness and the LPM spatial carrier. The PPM $\check{\zeta}$ is not affected by these artefacts.

VI. SUMMARY AND CONCLUSIONS

In this work we have introduced new methods for coherence imaging, a narrowband spectral imaging technique for diagnosing plasmas. This was motivated by wanting to maximize the quality and coverage of measurements of the divertor on the MAST-U spherical tokamak experiment. We applied the method of pixelated phase mask interferometry, already established in optics research, to CI, noting that it is more compact, rugged and can achieve a higher (average) spatial resolution than the existing linear phase mask methods. As well as a snapshot single-delay PPM CI instrument, we introduced a snapshot multi-delay instrument, suitable for measuring more complex spectra, that uses a combination of the PPM and LPM encodings.

We discussed in detail the application of CI to the measurement of electron density via Stark broadening of hydrogen Balmer line emission in plasma conditions relevant to the study of tokamak divertor physics. State-of-the-art lineshape calculations were incorporated into an LUT-based fitting procedure for inferring n_e from measurements of CI fringe contrast. Tests of this fitting procedure using synthetic data showed that the multi-delay instrument configuration can significantly widen the dynamic range of the n_e measurement by improving robustness against Doppler broadening effects at lower n_e. This allows n_e at the lower end of the anticipated MAST-U range ($5 \times 10^{19}\,\mathrm{m}^{-3}$) to be measured without significant systematic error.

Experimental CI measurements were made of divertor-relevant plasma conditions on the Magnum-PSI linear plasma experiment at DIFFER using single-delay and multi-delay CI instrument configurations. For measurements of H_γ emission, good agreement was found between the measured CI n_e profiles and those measured using Thomson scattering. Also, the predicted benefit of a multi-delay CI configuration was born out experimentally, as the multi-delay instrument could accurately measure down to at least $n_\mathrm{e} \sim 5 \times 10^{19}$ m^3 while accurate recovery of the beam profile below $n_\mathrm{e} \sim 10^{20}$ m^3 could not be achieved for the single-delay measurements without incorporation of other information. Estimates made of neutral temperature based on the multi-delay CI data were systematically higher than was reported for T_e by the TS system, which is consistent with previous spectroscopic studies on Pilot-PSI.

Modelling of CI measurements on the MAST-U divertor is also presented to demonstrate the lack of artefacts in the demodulated PPM fringe contrast image compared to an LPM image. Two CI instruments based on the PPM principles laid out in this paper are currently under development for the MAST-U tokamak.

ACKNOWLEDGMENTS

This work has been carried out within the framework of the EUROfusion Consortium and has received funding from the Euratom research and training programme 2014-2018 under grant agreement No 633053 and from the RCUK [grant numbers EP/T012250/1, EP/L01663X/1]. The views and opinions expressed herein do not necessarily reflect those of the European Commission. We would like to thank the team at Magnum-PSI for facilitating our experiments, in particular the help of Serje Brons, Thomas Morgan, Gijs Akkermans, Jack Leland and Fabio Federici. This work also benefited from conversations with Clive Michael, Chris Bowman, Sam Gibson and Joël Rosato.

Appendix A: Mueller matrices

The Mueller matrix for frame rotation from the x-axis towards the y-axis is[26]:

$$\mathrm{R}(\rho) = \begin{pmatrix} 1 & 0 & 0 & 0 \\ 0 & \cos(2\rho) & \sin(2\rho) & 0 \\ 0 & -\sin(2\rho) & \cos(2\rho) & 0 \\ 0 & 0 & 0 & 1 \end{pmatrix}. \tag{A1}$$

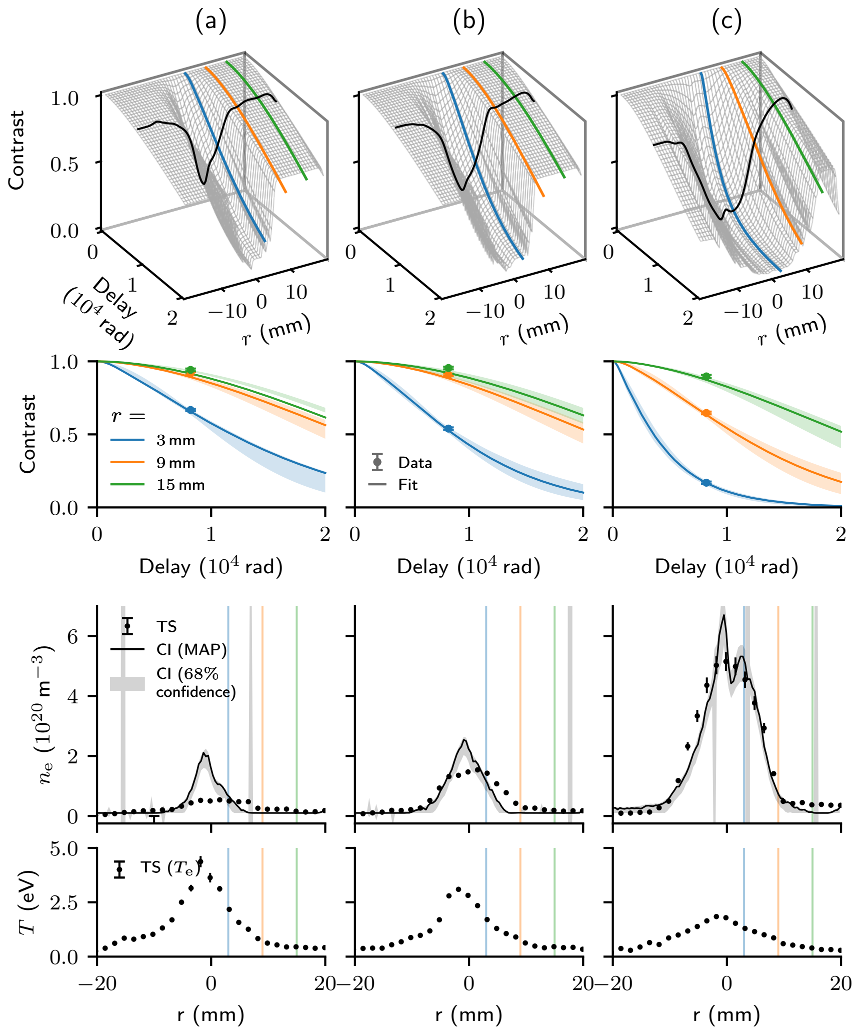

FIG. 9. Inverted single-delay CI results where columns (a)–(c) correspond to a scan from low to high n_e on Magnum-PSI. Source gas flow rate is $Q_s = 4.5$ SLM and $|B| = 1.5$ T for all discharges shown, while source current I_s is: (a) $I_s = 125$ A, (b) $I_s = 150$ A, (c) $I_s = 190$ A.

The Mueller matrix for an ideal linear polarizer, whose transmission axis makes an angle ρ with the x-axis is:

$$\mathrm{M_P}(\rho) \equiv \mathrm{R}(-\rho)\frac{1}{2}\begin{pmatrix}1 & 1 & 0 & 0\\ 1 & 1 & 0 & 0\\ 0 & 0 & 0 & 0\\ 0 & 0 & 0 & 0\end{pmatrix}\mathrm{R}(\rho). \tag{A2}$$

The Mueller matrix for an ideal linear retarder, whose fast axis makes an angle ρ with the x-axis is:

$$\mathrm{M_{LR}}(\rho,\phi) \equiv \mathrm{R}(-\rho)\begin{pmatrix}1 & 0 & 0 & 0\\ 0 & 1 & 0 & 0\\ 0 & 0 & \cos\phi & \sin\phi\\ 0 & 0 & -\sin\phi & \cos\phi\end{pmatrix}\mathrm{R}(\rho). \tag{A3}$$

It follows that the Mueller matrix for an ideal quarter-wave plate is $\mathrm{M_{QWP}}(\rho) \equiv \mathrm{M_{LR}}(\rho, \frac{\pi}{2})$.

[1] A. Loarte, B. Lipschultz, A. S. Kukushkin, G. F. Matthews, P. C. Stangeby, N. Asakura, G. F. Counsell, G. Federici, A. Kallenbach, K. Krieger, A. Mahdavi, V. Philipps, D. Reiter, J. Roth, J. Strachan, D. Whyte, R. Doerner, T. Eich, W. Fundamenski, A. Herrmann, M. Fenstermacher, P. Ghendrih, M. Groth, A. Kirschner, S. Konoshima, B. Labombard, P. Lang, A. W. Leonard, P. Monier-Garbet, R. Neu, H. Pacher, B. Pegourie, R. A. Pitts, S. Takamura, J. Terry, and E. Tsitrone, Nuclear Fusion **47** (2007), 10.1088/0029-5515/47/6/S04.

[2] W. Morris, J. R. Harrison, A. Kirk, B. Lipschultz, F. Militello, D. Moulton, and N. R. Walkden, IEEE Transactions on Plasma Science **46**, 1217 (2018).

[3] J. Howard, Applied Optics **41**, 197 (2002).

[4] J. Howard, Journal of Physics B: Atomic, Molecular and Optical Physics **43** (2010), 10.1088/0953-4075/43/14/144010.

[5] A. Perek, W. A. Vijvers, Y. Andrebe, I. G. Classen, B. P. Duval, C. Galperti, J. R. Harrison, B. L. Linehan, T. Ravensbergen, K. Verhaegh, and M. R. De Baar, Review of Scientific Instruments (2019), 10.1063/1.5115569.

[6] S. A. Silburn, *A Doppler Coherence Imaging Diagnostic for the Mega-Amp Spherical Tokamak*, Ph.D. thesis, Durham University (2014).

[7] S. A. Silburn, J. R. Harrison, J. Howard, K. J. Gibson, H. Meyer, C. A. Michael, and R. M. Sharples, Review of Scientific Instruments **85** (2014), 10.1063/1.4891165.

[8] C. M. Samuell, J. D. Lore, W. H. Meyer, M. W. Shafer, S. L. Allen, T. E. Evans, and J. Howard, Physical Review Research **2**, 1 (2020).

[9] V. Perseo, F. Effenberg, D. Gradic, R. König, O. P. Ford, F. Reimold, D. A. Ennis, O. Schmitz, and T. Sunn Pedersen, Nuclear Fusion **59** (2019), 10.1088/1741-4326/ab4320.

[10] D. Gradic, O. P. Ford, A. Burckhart, F. Effenberg, H. Frerichs, R. König, T. Lunt, V. Perseo, and R. C. Wolf, Plasma Physics and Controlled Fusion **60** (2018), 10.1088/1361-6587/aac4d2.

[11] T. Long, J. S. Allcock, L. Nie, R. M. Sharples, M. Xu, R. Ke, S. Zhang, S. A. Silburn, J. Howard, Y. Yu, B. Yuan, Z. H. Wang, X. M. Song, L. Liu, and X. R. Duan, Review of Scientific Instruments (2020), 10.1063/5.0005609.

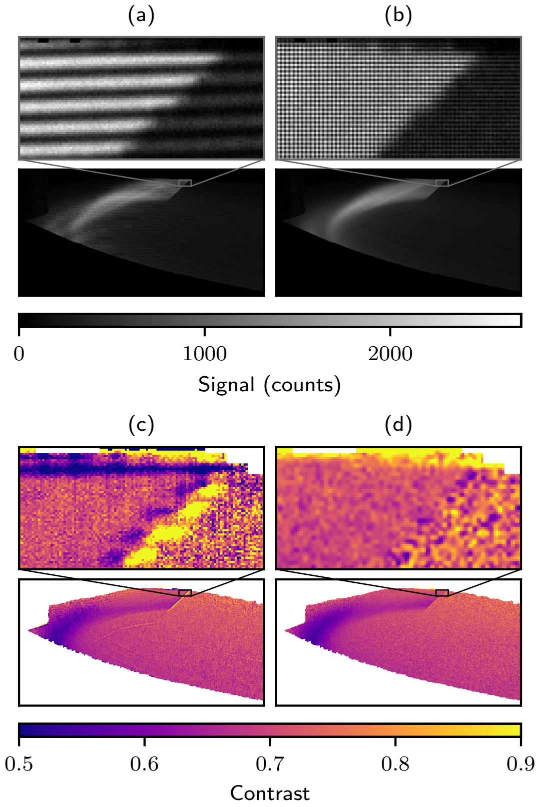

FIG. 10. Synthetic CI images viewing H_γ emission from the MAST-U divertor generated using CHERAB for (a) a linear phase mask and (b) a pixelated phase mask. (c) and (d) show the corresponding demodulated fringe contrast images.

[12] B. A. Lomanowski, A. G. Meigs, R. M. Sharples, M. Stamp, and C. Guillemaut, Nuclear Fusion **55** (2015), 10.1088/0029-5515/55/12/123028.

[13] J. R. Harrison, S. W. Lisgo, K. J. Gibson, P. Tamain, J. Dowling, and The Mast Team, in *Journal of Nuclear Materials*, Vol. 415 (2011).

[14] K. Verhaegh, B. Lipschultz, B. P. Duval, J. R. Harrison, H. Reimerdes, C. Theiler, B. Labit, R. Maurizio, C. Marini, F. Nespoli, U. Sheikh, C. K. Tsui, N. Vianello, and W. A. Vijvers, Nuclear Materials and Energy **12**, 1112 (2017), arXiv:1607.04539.

[15] S. Potzel, R. Dux, H. W. Müller, A. Scarabosio, and M. Wischmeier, Plasma Physics and Controlled Fusion **56** (2014), 10.1088/0741-3335/56/2/025010.

[16] I. H. Hutchinson, *Principles of Plasma Diagnostics* (2002) arXiv:arXiv:1011.1669v3.

[17] O. Lischtschenko, K. Bystrov, G. De Temmerman, J. Howard, R. J. Jaspers, and R. König, Review of Scientific Instruments **81**, 1 (2010).

[18] G. De Temmerman, M. A. Van Den Berg, J. Scholten, A. Lof, H. J. Van Der Meiden, H. J. Van Eck, T. W. Morgan, T. M. De Kruijf, P. A. Zeijlmans Van Emmichoven, and J. J. Zielinski, in *Fusion Engineering and Design*, Vol. 88 (2013) pp. 483–487.

[19] J. E. Millerd, N. J. Brock, J. B. Hayes, M. B. North-Morris, M. Novak, and J. C. Wyant, Interferometry XII: Techniques and Analysis **5531**, 304 (2004).

[20] K. Creath and G. Goldstein, Biomedical Optics Express **3**, 2866 (2012).

[21] T. Tahara, R. Yonesaka, S. Yamamoto, T. Kakue, P. Xia, Y. Awatsuji, K. Nishio, S. Ura, T. Kubota, and O. Matoba, IEEE Journal on Selected Topics in Quantum Electronics **18**, 1387 (2012).

[22] K. Ishikawa, K. Yatabe, N. Chitanont, Y. Ikeda, Y. Oikawa, T. Onuma, H. Niwa, and M. Yoshii, Optics Express (2016), 10.1364/oe.24.012922.

[23] M. Francon and S. Mallick, *Polarization Interferometers* (Wiley-Interscience, 1971).

[24] W. H. Steel, *Interferometry*, 2nd ed. (Cambridge University Press, 1987).

[25] M. P. Kothiyal and C. Delisle, Applied Optics **24**, 4439 (1985).

[26] R. A. Chipman, W.-S. T. Lam, and G. Young, *Polarized Light and Optical Systems* (2018).

[27] C. A. Michael, J. Howard, and B. D. Blackwell, Physics of Plasmas (2004), 10.1063/1.1768175.

[28] F. E. Veiras, L. I. Perez, and M. T. Garea, Applied Optics **49**, 2769 (2010).

[29] B. Kimbrough and J. Millerd, Interferometry XV: Techniques and Analysis **7790**, 77900K (2010).

[30] M. Servin, J. A. Quiroga, and M. Padilla, *Fringe Pattern Analysis for Optical Metrology: Theory, Algorithms, and Applications* (Wiley-VCH, 2014) pp. 177–186.

[31] C. M. Samuell, S. L. Allen, W. H. Meyer, and J. Howard, Journal of Instrumentation **12** (2017), 10.1088/1748-0221/12/08/C08016.

[32] P. Urlings, "Multiple Delay Coherence Imaging Charge Exchange Recombination Spectroscopy (MSc thesis)," Tech. Rep. (Eindhoven University of Technology, 2015).

[33] D. J. Bone, H.-A. Bachor, and R. J. Sandeman, Applied Optics **25**, 1653 (1986).

[34] J. Rosato, Y. Marandet, and R. Stamm, Journal of Quantitative Spectroscopy and Radiative Transfer **187**, 333 (2017).

[35] J. Rosato, "Private communication,".

[36] S. Trippe, Journal of the Korean Astronomical Society **47**, 15 (2014), arXiv:1401.1911.

[37] A. E. Shumack, V. P. Veremiyenko, D. C. Schram, H. J. De Blank, W. J. Goedheer, H. J. Van Der Meiden, W. A. Vijvers, J. Westerhout, N. J. Lopes Cardozo, and G. J. Van Rooij, Physical Review E - Statistical, Nonlinear, and Soft Matter Physics (2008), 10.1103/PhysRevE.78.046405.

[38] D. S. Sivia and J. Skilling, *Data Analysis: A Bayesian Tutorial* (Oxford University Press, 2006).

[39] H. J. Van Der Meiden, A. R. Lof, M. A. Van Den Berg, S. Brons, A. J. Donné, H. J. Van Eck, P. M. Koelman, W. R. Koppers, O. G. Kruijt, N. N. Naumenko, T. Oyevaar, P. R. Prins, J. Rapp, J. Scholten, D. C. Schram, P. H. Smeets, G. Van Der Star, S. N. Tugarinov, and P. A. Van Emmichoven, Review of Scientific Instruments **83** (2012), 10.1063/1.4768527.

[40] A. H. Andersen and A. C. Kak, Ultrasonic Imaging (1984), 10.1177/016173468400600107.

[41] M. Carr, A. Meakins, A. Baciero, M. Bernert, A. Callarelli, A. Field, C. Giroud, J. Harrison, N. Hawkes, S. Henderson, B. Lipschultz, T. Lunt, D. Moulton, and F. Reimold, in *44th EPS Conference on Plasma Physics, EPS 2017* (2017).

[42] M. Carr, D. A. Meakins, M. Tomes, and vsnever, "cherab/core: Release v1.2.0," (2019).

[43] J. R. Harrison, D. Moulton, M. Carr, I. T. Chapman, D. Keeling, A. Kirk, and N. R. Walkden, in *43rd European Physical Society Conference on Plasma Physics, EPS 2016* (2016).

[44] "https://www.sony-semicon.co.jp/e/products/IS/industry/product/polarization.html,".

[45] C. M. Samuell, S. L. Allen, W. H. Meyer, R. C. Isler, A. Briesemeister, R. S. Wilcox, C. J. Lasnier, A. G. McLean, and J. Howard, Review of Scientific Instruments **89** (2018), 10.1063/1.5039367.